Fatigue of fiber-metal-laminates with aluminum core, CFRP face sheets and elastomer interlayers (FMEL)

Matthias M. Stoll, Kay A. Weidenmann

Angaben zur Veröffentlichung / Publication details:

Stoll, Matthias M., and Kay A. Weidenmann. 2018. "Fatigue of fiber-metal-laminates with aluminum core, CFRP face sheets and elastomer interlayers (FMEL)." *International Journal of Fatigue* 107: 110–18. https://doi.org/10.1016/j.ijfatigue.2017.10.017.

Fatigue of fiber-metal-laminates with aluminum core, CFRP face sheets and elastomer interlayers (FMEL)

Matthias M. Stoll*, Kay A. Weidenmann

Karlsruhe Institute of Technology (KIT), Institute for Applied Materials – Material Science and Engineering (IAM-WK), Department Hybrid and Lightweight Materials, Kaiserstraße 12, 76131 Karlsruhe, Germany

1. Introduction

Fiber-Metal-Laminates (FML) are currently used in aviation, as many new aircrafts feature an FML in large parts of the load bearing structure [1]. The most prominent FML is GLARE, a glass fiber reinforced epoxy paired with aluminum 2024-T3 sheets [2–4]. The benefits of this new material are dynamic resistances such as a high fatigue resistance and an extraordinary resistance to crack propagation [5–7]. However, the stiffness of the system is reduced compared to bulk aluminum. To obtain a higher stiffness of an FML, one possibility would be to substitute the glass fibers with carbon fibers. Thus, increasing the laminate's overall stiffness, while reducing its density. Additionally the CFRP can be placed in the face sheet, thus using the moment of inertia to increase the laminate stiffness.

Carbon fiber reinforced aluminum laminates (CARALL) generally feature a high difference in the constituent's coefficient of thermal expansion (CTE-mismatch) and the possibility of galvanic corrosion [8–10]. These problems may be solved by integration of elastomer interlayers. The elastomer inhibits corrosion through a high electrical resistance and uses high elastic strains to absorb the CTE-mismatch, while it is desired to increase adhesion. Elastomer interlayers were already used in different laminate structures, with either carbon or glass fibers, to increase damping, adhesion and the resistance to corrosion [11–15].

CARALL research often showed that the laminate is not suitable for application due to the reasons presented above [16]. To circumvent the problems of CARALL laminates were fabricated, where the metal sheet was substituted with a less corrodible metal like titanium [17] or a polymer interlayer was applied to ensure adhesion [16]. However, no extensive fatigue tests were performed on those laminates [18–20]. More extensive research under fatigue loading was carried out using the more prominent GLARE [21–32].

Fatigue experiments on composites are essential for the applicability in dynamically loaded structures. The complex behavior, due to effects like fiber bridging and matrix fracture in 90° plies, has to be experimentally proven [22,23]. During fatigue loading, damping in the polymer layer induces heat into the specimen, thus making it necessary to monitor the temperature during the experiment [24]. The material in this study consists of CFRP, elastomer and aluminum layers, but the interactions of the constituents are crucial for the laminate's performance, as delamination could cause premature failure. Fatigue in FMLs has already been researched, but the main focus was on the crack propagation and therefore notched specimens were used [25–32]. However, since the stiffness degradation is investigated in this study notch-free coupon specimens were tested. The research already conducted examined the crack growth and cannot be transferred to different damage mechanisms in bulk fatigue testing. The differences in constituent materials and specimen geometry additionally render the transferability of the research to this study futile. The loading rate was low to inhibit internal heating caused by damping of the polymer

* Corresponding author.
E-mail addresses: Matthias.Stoll@kit.edu (M.M. Stoll), Kay.Weidenmann@kit.edu (K.A. Weidenmann).

components. The load was set according to ISO 13003 [33]. As failure criterion, a 20% stiffness degradation was chosen. It was assumed that with this stiffness drop, the functionality of the structure can not be assured.

The damage evolution in FRP and metals is well described, and lifetime prediction theories are established for each material. For the aluminum core the lifetime can be predicted using the Coffin-Manson [34] or Basqiun [35] relation depending on the cycles to failure. The effect of the mean stress can be considered with the Goodman or Gerber model [36]. The elastomer interlayer is not expected to fracture, because the maximum strain of the elastomer will not be reached at the failure of the laminate. A lifetime prediction for CFRP specimens has a variety of approaches: Either the unidirectional layup is considered [37] or multiaxial sheets were predicted [38]. The stress ratio also factors into the lifetime prediction [39–41]. If the failure criterion of stiffness reduction is chosen, the prediction has to be adapted [42,43]. As stated before, the properties of the constituents cannot be simply superimposed, but the interaction of the constituents have to be taken into account. Therefore, the damage evolution in the specimen was monitored by X-ray computed tomography (CT-scans) [44–46]. The aluminum layer is expected to cause beam hardening and the sample size are expected to prevent detection of single carbon fibers.

2. Material and methods

Fiber-Metal-Laminates with elastomer interlayers (FMEL) consist of CFRP face layers, elastomer interlayers and an aluminum core. The layup of the laminate investigated in this study was symmetrical to inhibit warpage caused by the CTE-mismatch combined with the cooling from processing temperature. The FMEL specimens were manufactured at the Institute for Production Science (wbk) at the Karlsruhe Institute of Technology (KIT). A Lauffer type RP 400 OK 920 machine press was used. The laminates were manufactured at 150 °C and 23 bar pressure, the curing cycle duration was 300 s.

2.1. Carbon fiber reinforced polymer (CFRP)

The CFRP used in this study was a Hexcel “M77/42%/UD90/CHS” prepreg with unidirectional high strength carbon fibers and an optimized resin for fast curing cycles to counteract the usually long production cycles of FML [22,47]. For the application in the FMEL a low sheet thickness of 0.1 mm was essential to guarantee a variable layup of the CFRP’s properties in the laminate. The 0.1 mm thick prepreg allows layups with different directions to form the resulting CFRP layer; in this study a biaxial layup was used. The curing temperature of the epoxy matrix of 150 °C was matched to the curing temperature of the elastomer interlayer to ensure good polymerization [48]. Due to the high strength carbon fibers and a fiber volume content of approximately 50% the CFRP had high mechanical properties. The density was 1.5 g/cm^3, the Young’s Modulus of the unidirectional CFRP sheet was 120 GPa and the tensile strength 2250 MPa. The stiffness perpendicular to the fibers was 3 GPa. The unidirectional prepreg sheets were arranged to a biaxial CFRP layer with 0.6 mm thickness.

2.2. Aluminum

The metal examined in this study was selected according to high resistance to sheet bending combined with a low density and the restriction of commercial availability in 0.3 mm thin sheets. Aluminum 2024-T3 fits all requirements and has the benefit of comparability, as many FML use this alloy [1,2]. The mechanical properties of the aluminum alloy were taken from tensile tests carried out with aluminum sheet specimens. The Young’s Modulus was 73 GPa, the yield strength was 320 MPa and the tensile strength was 435 MPa.

2.3. Elastomer

The elastomer used in this research was provided by Kraiburg Holding GmbH & Co. KG, Waldkraiburg, Germany. The elastomer’s registered trade name is Kraibon. It is optimized for applications with CFRP. The chosen mixture, SAA-9579/52, did not only possess enhanced adhesion to CFRP with epoxy matrix but also to aluminum. The elastomer interlayer promised inhibited corrosion, a balanced CTE-mismatch and increased adhesion. The elastomer layer had a thickness of 0.5 mm and its curing temperature fit the curing temperatures of the Hexcel M77/42%/UD90/CHS. The curing cycle time for the FMEL was defined by the elastomer, as it was the slower curing component of the laminate. The resulting cycle time was 300 s at 150 °C. The elastomer interlayer was introduced to inhibit corrosion by electrical decoupling and to balance the CTE-mismatch through high ductility. Additionally the adhesive properties of the elastomer were intended to increase interfacial properties. With increasing thickness these effects were strengthened, but mechanical properties, like bending stiffness, were reduced. A thickness of 0.5 mm was chosen to guarantee corrosion resistance and CTE-mismatch balancing, but retain the mechanical properties at a high level.

2.4. Laminate

Fig. 1 shows the layup of the FMEL consisting of 5 layers of constituents optimized for sheet bending. The CFRP face layers, each consisting of 6 uni-directional CFRP prepreg layers, are the primary load bearing structure in the laminate. They were situated close to the outer fiber of the specimens to optimize the bending stiffness [49]. The integration of aluminum introduces interfaces, which function as obstacles for crack propagation, thus increasing dynamic properties. The elastomer interlayer promises good adhesion, inhibition of corrosion and balancing of the CTE-mismatch through high strains.

The material’s selection resulted in this layup as desirable for lightweight sheet materials with high flexural stiffness when using the three given materials [50]. The stiffness to weight ratio was optimized, while the laminate’s thickness was set to 2.5 mm. The optimum laminate consisted of 0.6 mm CFRP face layers, 0.5 mm elastomer interlayers and a 0.3 mm aluminum core.

Fig. 2 presents the structure of the laminate. The CFRP face layer with different fiber orientations depending on the unidirectional layer are visible. The adhesively bonded elastomer connects the CFRP and aluminum.

2.5. Lifetime prediction

The constituent failure was predicted individually and superimposed to predict laminate failure. The failure in the aluminum sheet was predicted using the Coffin-Manson equation and the CFRP constituents stiffness reduction was calculated likewise to Ogin et al. [42]. The elastomer was assumed to stay intact throughout the experiment and failure of the specimen, because the laminate’s strain at failure is lower compared to the elastomer’s maximum strain.

The lifetime predictions were calculated and damages in the layers predicted. Thus, the current stress distribution was recalculated and the laminate prediction was updated. At the failure of one component, the stress in the other components was increased, which changed the

Fig. 1. FMEL specimen with CFRP face layers, aluminum core and elastomer interlayer.

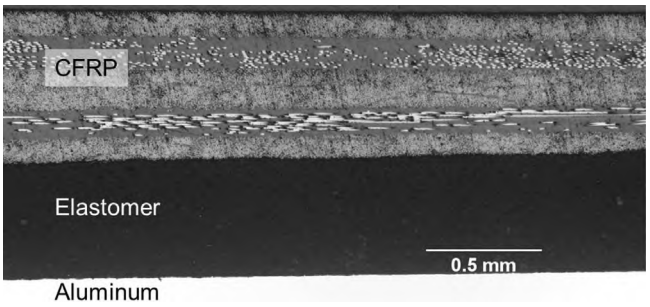

Fig. 2. Cross-section polish of three layers of an FMEL.

lifetime prediction. The laminate's lifetime was predicted by using the predictions of the components at varying stress levels, depending on the damage and stress distribution in the laminate.

2.5.1. Lifetime prediction of the aluminum sheet

The lifetime prediction for the aluminum sheet was carried out using the Coffin-Manson approach (cf. Eq. (1)). The stress applied to the aluminum was calculated assuming constant strain in the constituents.

$$\frac{\Delta \epsilon_{pl}}{2} = \epsilon'_f \, (N_B)^c \tag{1}$$

$\frac{\Delta \epsilon_{pl}}{2}$ is the plastic strain amplitude, ϵ'_f is the strain at failure, N_B are the cycles to failure and c is the fatigue ductility coefficient.

The fatigue ductility coefficient was approximated using the true strain at failure. $\epsilon_{true,B} \approx \epsilon'_f = 12.5\%$ was taken from quasi-static tensile tests of the aluminum sheet. A generally approximated fatigue ductility exponent for ductile metals was used at $c = -0.6$.

2.5.2. Lifetime prediction of the CFRP constituent

The lifetime of the CFRP constituent is largely determined by matrix cracking of the 90° plies. Since the stiffness reduction was chosen as failure criterion, the corresponding stiffness reduction in the CFRP layer had to be predicted. The following Eq. (2) was taken from Ogin et al.:

$$-\frac{1}{E_0}\frac{dE}{dN} = A\left[\frac{\sigma^2_{max}}{E_0^2(1-E/E_0)}\right]^n \tag{2}$$

E_0 is the initial Young's Modulus and $\frac{dE}{dN}$ is the change in Young's Modulus. A and n are constants, which have to be obtained from fatigue experiments. σ_{max} is the maximum applied stress and E is the current Young's Modulus.

A plot of Eq. (2) is shown in Fig. 4, where the values for A and n could be deduced. The figure shows the data points of the laminates at high load levels. The low cycle fatigue experiments were used to predict the fatigue endurance of the laminate. The loads for the CFRP layer were approximated with a fractured aluminum layer, because failure was predicted early compared to the CFRP component.

3. Experimental

The characteristics of fatigue loading, for example the loading in pure tension or tension-compression, generally change the material's resistance. FRPs show micro-buckling of the fibers in compression load, resulting in premature failure. The CFRP is the primarily load bearing structure and so tension-tension fatigue is the experiment chosen to prevent premature failure due to micro-buckling.

The load levels for fatigue testing are percentiles of the ultimate tensile strength (UTS), which was determined before fatigue testing (cf. Section 3.1). Most components are designed using the material's stiffness. However, the stiffness of CFRP can decrease during the lifetime. Thus, the failure criterion 20% stiffness reduction was chosen over specimen separation.

Table 1
Strain rates of the different load levels.

Percentile of UTS (%)	Stress amplitude (MPa)	Strain rate (%/s)
40	60	2.4
55	82.5	3.3
80	120	4.8

3.1. Ultimate tensile strength (UTS)

The UTS describes the tensile strength, but factors in the strain rate, which is different in fatigue and quasi-static experiments. The UTS was determined using tensile tests according to ISO 527-5 [51]. However, the strain rate of the fatigue experiments was used. The strain rate results from the testing frequency and the maximum stress for each load level as presented in Table 1.

A ZwickRoell ZMART.PRO 200 kN universal testing machine with MultiXtens and hydraulic grippers were used. The applied frequency resulted in the loading rates presented in Table 1.

3.2. Tension-tension fatigue

The specimens used for fatigue testing were coupon specimens with the dimensions 250 mm × 25 mm × 2.5 mm. The specimens were cut by water jet cutting. Aluminum cap strips were not necessary, except for the specimen used for CT-monitored damage evolution. These specimens were mounted repeatedly and therefore needed reinforcement in the gripper area to prevent premature failure. The 1 mm thick aluminum cap strips were glued on the sample by the adhesive Uhu Endfest 300 and cured at ambient temperature for 24 h.

The experiments were stress controlled with a constant frequency of 5 Hz, while the strain and temperature were measured. The load levels relative to UTS were set according to the standard at 40%, 55% and 80% and the failure criterion was a stiffness reduction of 20%. For these experiments no cap strips were necessary. A servo hydraulic testing machine with flat hydraulic grippers was used for fatigue testing. The predetermined stress was a sinusoidal wave with a given mean stress, which was set relative to the UTS.

3.3. Stiffness degradation

Fiber reinforced polymers show a damage accumulation under fatigue loading, although there is no specimen separation, the stiffness decreases significantly. This effect is primarily caused by matrix cracking of the 90° plies while the specimens remain macroscopically intact. When examining metals the failure criterion is often specimen separation. However, in this study a stiffness reduction of 20% was used, because of the large impact of the CFRP component.

The CFRP constituent could cause the stiffness decrease in the FMEL, but also a fracture of the aluminum sheet could result in a stiffness reduction. The fractured aluminum layer was able to carry load after fracture, because the elastomer could introduce and distribute load. In the case of an aluminum fracture the stiffness would spontaneously decrease significantly. The damage leading to a decrease in mechanical properties is therefore observed by CT-imaging and thermal measurements to determine whether the failure was induced by the FRP or the aluminum constituent. The temperature accumulation caused by damage in the laminate was monitored using thermal imaging.

3.4. CT-imaging

For CT-imaging a Yxlon Y.CT Precision μCT with a detector resolution of 2048 pixels × 2048 pixels was used. The specimen was mounted using a polymer clamp without mechanical load. The scan was carried out using 2700 projections at a acceleration voltage of 90 kV

and 0.47 mA current. The CT-imaging was carried out for selected specimens, as the experiment had to be stopped for scanning. Due to multiple mounting of the specimens, the gripper area was reinforced with aluminum cap strips. The scanning occurred prior to the experiments to generate a reference and after each 1000 cycles, while comparing the scan to the reference data. The CT-scans were used to define the damage mechanism in the laminate and to assign the stiffness decrease to a constituent.

3.5. Temperature monitoring

The polymer components show temperature-dependent characteristics and therefore the specimen's temperature increase due to internal friction was monitored to be able to deduce mechanical properties and to ensure comparability. An increase in temperature could cause the properties to change, preventing any conclusion about the laminates behavior and damage evolution.

The thermal imaging device was a FLIR T420 Infrared Camera, which was used to monitor the specimen's temperature and compare it to the 5 °C threshold in ISO 13003.

A transgression of the threshold would have caused the experimental frequency to be lowered and rendered any results at the initial frequency inconclusive.

In terms of damage evolution it is of interest to detect areas of higher temperature and correlate them with damage in the specimens. Areas with accumulated damage in the specimens result in higher stress in the intact constituents in this area. Therefore a higher temperature could indicate localized damage in the laminate. Post mortem CT imaging is intended to link the hot spots during the experiment to laminate damage. The experimental procedure is described in Chapter 3.4.

4. Results

The results of this study will be described focusing on the results concerning the lifetime prediction, the S-N-curve and the UTS. Another focus was the damage evolution observed by CT-scans and temperature monitoring, which was linked to change in the mechanical properties.

4.1. Lifetime prediction

The lifetime prediction for the aluminum core layer was carried out according to Coffin-Manson. The resulting cycles to failure for the aluminum are presented in Table 2:

The low cycle numbers indicate, that the aluminum is not expected to endure the fatigue experiments, but fracture in the process. The fatigue endurance therefore had to be determined for the CFRP constituent.

The lifetime prediction for the CFRP constituent was carried out according to Ogin et al. [42]. The higher stresses after the aluminum fracture were already considered in the CFRP lifetime prediction to generate a laminate prediction.

Eq. (2) can be plotted using data points of fatigue experiments. Fig. 3 shows the experimentally obtained data points and the linear fit. The coefficients $A = 30365908$ and $n = 3{,}90147$ were taken from the diagram through fitting of a straight line. By integration of equation with the coefficients obtained from the low cycle fatigue specimens, the

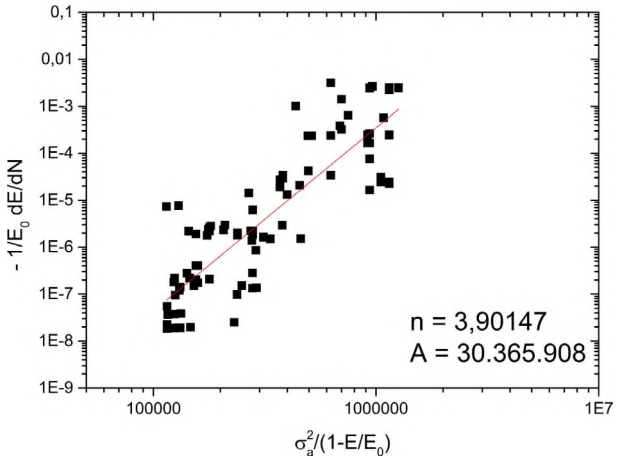

Fig. 3. Diagram for the determination of A and n from experimental data by a linear fit.

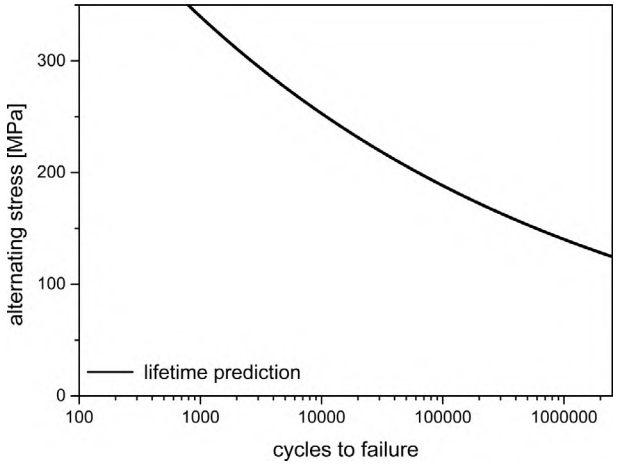

Fig. 4. The lifetime prediction for the desired stiffness reduction of the CFRP.

lifetime prediction can be calculated.

Fig. 4 shows the resulting prediction for a S-N curve for the CFRP, which was calculated from experimentally obtained data. The line plotted in Fig. 4 is shown in Eq. (3).

$$\frac{E}{E_0} = 1 - \left(46{,}5 * \left(\frac{\sigma_{max}}{E_0}\right)^{1{,}6} * N^{0{,}2}\right) \tag{3}$$

The lifetime prediction overestimates the low cycle performance, as it predicts values higher than the tensile strength. The fatigue limit at 2 million cycles is 128.25 MPa.

4.2. Ultimate tensile strength

The ultimate tensile strength, which is the strength at the strain rate of the fatigue experiment, was experimentally determined with 5 specimens. $\sigma_{max} = 333$ MPa ± 27 MPa The load levels for the fatigue testing are calculated for mean and alternating stresses as shown in Table 3.

Table 2
Lifetime prediction for the aluminum sheet in the FMEL.

Load level (%)	Cycles to failure
40	27706
55	3941
80	824

Table 3
Load levels and stress levels of the FMEL fatigue experiments.

Load level	Mean stress (MPa)	Alternating stress (MPa)
80% of UTS	145	120
55% of UTS	100	82.5
40% of UTS	73	60

Fig. 5. The upper FMEL specimens was depicted before and the lower specimen after fatigue loading.

4.3. Fatigue properties

The S-N curve in this study was a result of tension-tension fatigue testing at R = 0.1 and load levels according to ISO 13003. The FMEL specimens are presented in Fig. 5. The upper specimen was not yet loaded, whereas the lower specimen already endured the fatigue loading. Since the failure criterion is stiffness reduction, the specimens did not separate.

The stiffness reduction was calculated using the relative dynamic modulus, which was obtained by division of the current modulus throughout the experiment by the initial modulus. The failure criterion was met when the current modulus fell below 80% of the initial value.

Fig. 6 shows a plot of the relative dynamic Young's Modulus and the failure criterion at the load level of 55% of UTS measured during the experiment. The relative dynamic Young's Modulus is calculated by division of the current dynamic Young's Modulus with the initial dynamic Young's Modulus. The modulus is almost constant until approximately 3 000 cycles. A stiffness degradation is visible and eventually reaching the failure criterion at approximately 90 000 cycles. This curve is representative for all specimens.

The initial stiffness decrease between approximately 3000 and 10,000 cycles was correlated with the fracture of the aluminum core sheet. The damage of the aluminum layer occurred over a span of cycles and resulted in a steep stiffness decrease. Although the diagram is logarithmic, the initial stiffness decrease is more prominent than the transverse matrix cracking at higher cycles.

The S-N curve presented in Fig. 7 shows the known characteristics, which can be divided into fatigue strength and fatigue endurance limit. It shows a failure probability of 50%. The fatigue endurance limit was reached at 40% of the UTS, even with the stiffness degradation failure criterion. In the low cycle fatigue area, the curve in Fig. 7 shows high scattering at high load levels.

4.4. Temperature monitoring

The temperature measurements were carried out at the highest load

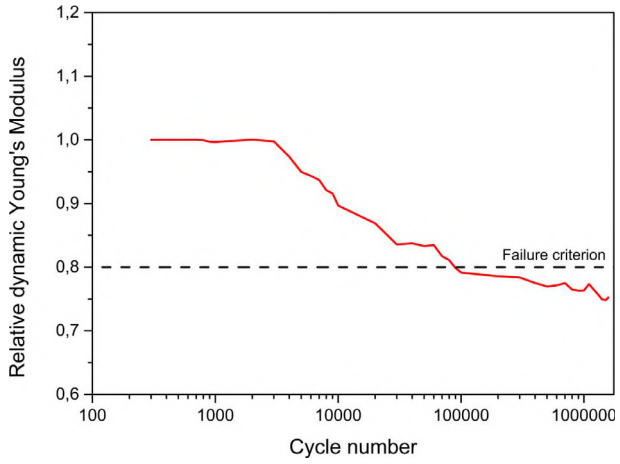

Fig. 6. Relative dynamic Young's Modulus at 55% of UTS.

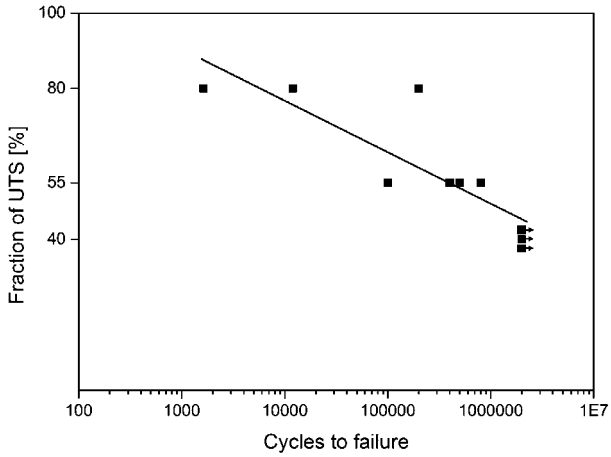

Fig. 7. 50% failure probability S-N curve for FMEL with the failure criteron of 20% stiffness reduction.

level, because at this load level the heat accumulation due to friction was maximized. It was possible to detect hot spots by thermal imaging, which could represent damage to the laminate. The temperature accumulated by the specimens is shown in Fig. 8. The temperature increased 2 °C, but then reached a limit (see Fig. 9).

Fig. 8 shows specimen temperatures before loading, after approximate cycle numbers of 1000; 10,000 and 100,000. A limit of the heat generation can be observed, which is reached shortly after the start of the experiment. After 1000 cycles a stiffness drop was detected. This damage to the laminate induced heat due to friction and higher stresses. The temperature threshold was not met at the failure criterion.

Regions with elevated temperature could be detected, where the friction in the polymer was higher. The higher friction could be caused by locally higher stress in the CFRP component. The higher stress could have resulted from the failure of one constituent and stress redistribution into the CFRP layer. The indicated locations were examined for damage in the laminate with CT-scans, because aluminum fracture was expected at these locations. The initial area with higher temperature was at the lower part of the specimen, but in the last picture a second area with damage is visible in the center of the specimen. Therefore multiple cracks in the aluminum were expected.

The temperature-time plot shows that the specimen temperature rose quickly after the experiment was started, but then reached an equilibrium between heat generation and distribution. The temperature increase was approximately 2 °C, but well below the 5 °C threshold required for testing according to ISO 13003.

4.5. CT-imaging

CT-imaging was used to detect damage. Because damage in fatigue experiments occurs throughout the testing, the fatigue experiment had to be paused to scan the specimens. Fig. 10 shows the stiffness of the specimen with the pauses of the experiment after every 1000 cycles. The specimen was scanned at every pause. The intact specimen is shown in Fig. 11(a) with different colors for the constituents.

The first damage occurred after 5 000 cycles, as it is visualized in the stiffness decrease in Fig. 10. To monitor the damage of the laminate only the significant layers were visualized, thus in Fig. 11(b) only the aluminum layer is visible. A crack through the aluminum constituent is visualized in the scan. Therefore, the sudden stiffness decrease in the fatigue experiment indicated the fracture of the aluminum.

The following stiffness evolution is monotonously decreasing without sharp drops. It is caused by transverse cracks in the matrix and single fiber fractures. However, due to the specimen width of 25 mm and the beam hardening, no single fiber or matrix cracks could be monitored. The beam hardening cast a shadow over the damages in the

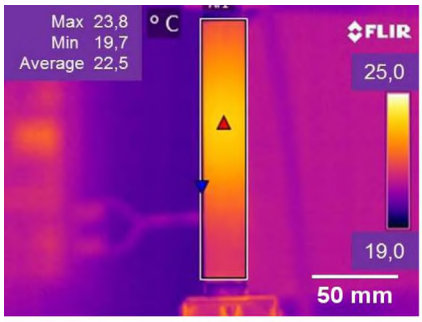

(a) Before loading

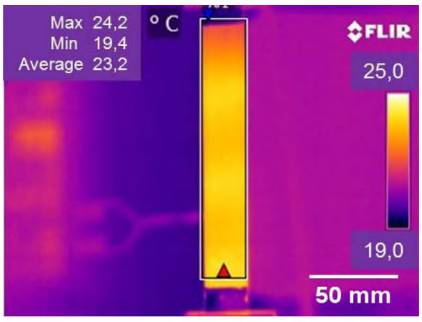

(b) After 1 000 cycles

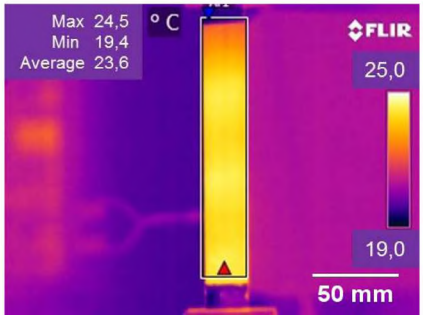

(c) After 10 000 cycles

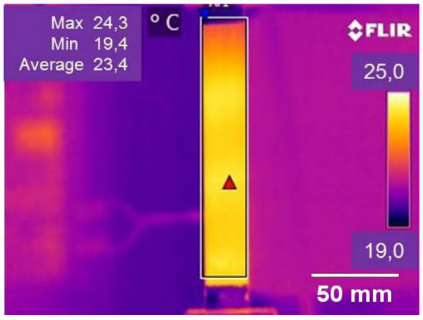

(d) After 100 000 cycles

Fig. 8. Thermal images of fatigue specimen at 80% load level after specific cycle numbers with the red and blue triangles indicating the hottest and coldest spot of the specimen. (For interpretation of the references to colour in this figure legend, the reader is referred to the web version of this article.)

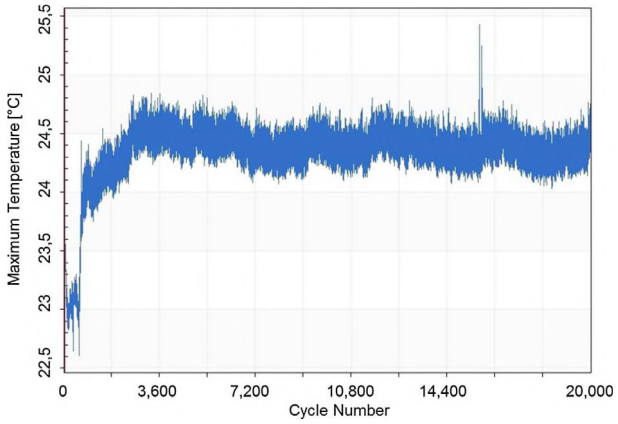

Fig. 9. Temperature versus Time plot of the fatigue specimen to cycle 20 000 at 80% UTS.

CFRP, preventing detection of the differences in absorption.

The specimen shown in Fig. 11(a) was scanned before loading it for the first time as shown in Fig. 10. After scanning it was loaded with 1000 cycles at 55% of UTS and the CT-scan was repeated. This procedure was carried out for 10,000 cycles, respectively 10 CT-scans.

Fig. 10 illustrates the relative stiffness of the specimen during the fatigue test.

5. Discussion

The fatigue experiments on FMEL showed cracks in the aluminum layer, which was detected by CT-imaging (cf. Fig. 11(b)). Additionally the thermal imaging detected areas of higher temperatures, where cracks could be found after the experiment. The S-N curve was deduced against a stiffness decrease failure criterion.

5.1. Fatigue experiments

The damage in FMEL under fatigue loading was observed using CT-scans and thermal imaging assisting the mechanical measurements. The specimens showed no detectable damage at the lowest load level of 40% of UTS, setting the fatigue endurance limit. ISO 13003 postulates a lower load level at 25%, which was omitted. The medium and high load levels of 55% respectively 80%, however, showed aluminum fractures in CT-scans and areas of higher temperature in thermal images.

At the 55% load level cracks were detected using CT-scans. The cracks occurred in the aluminum component of the laminate, while the other laminate constituents remained intact. The fracture in the aluminum component caused most prominent stiffness decrease in Fig. 6.

Fig. 12 compares the Coffin-Manson lifetime prediction with the experimentally gathered results. The aluminum fracture was associated with a large and sharp stiffness decrease during the experiment. The prediction fit the experimental results.

The failure of the aluminum did not cause the laminate to meet the failure criterion. Also no delamination occurred due to the elastomer layer. Without the elastomer layer delamination would occur prior or after the aluminum fracture, which would reduce the lifetime of the laminate. The lifetime prediction of the aluminum was not significant enough to describe the laminate's fatigue performance. The laminate's stiffness decrease was primarily caused by transverse matrix cracking in the 90° plies of the CFRP. The damage of the aluminum and the CFRP combined result in the stiffness degradation of the laminate. The aluminum damage is a fracture through the whole layer as visualized in Fig. 11(b). The transverse cracks in the CFRP could not be monitored by CT imaging, because the beam hardening of the aluminum overshadowed the cracks. Matrix cracks and single fiber failure could not be visualized by CT-scans due to the cone beam, which set the minimum voxel size higher than the width of the matrix cracks or the diameter of the carbon fibers.

Fig. 13 shows that the lifetime prediction generally underestimates the performance of the laminate. Except for one value, the prediction is conservative. The values of the prediction fit the experiment

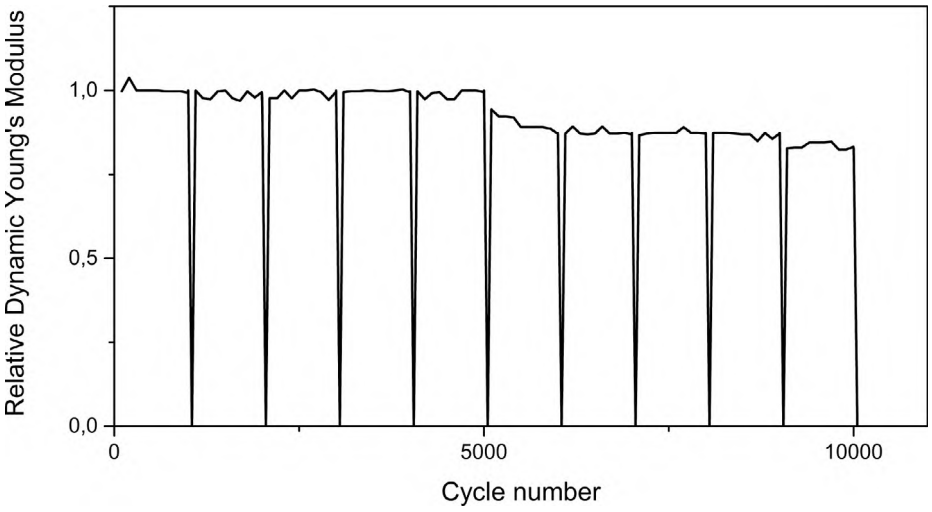

Fig. 10. Stiffness evolution of a specimen used for CT imaging.

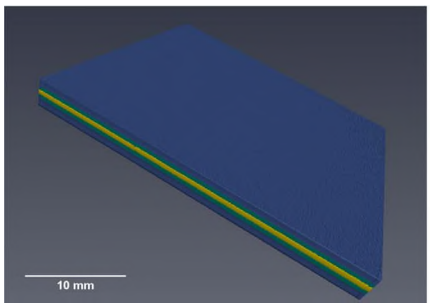

(a) 5-layer laminate

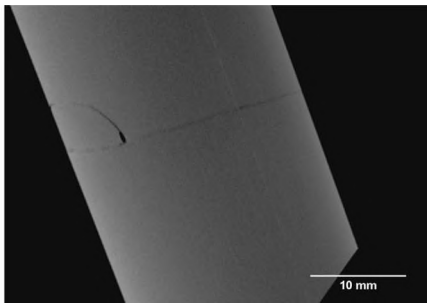

(b) aluminum layer of the laminate

Fig. 11. 3D-model of the laminate with blue representing CFRP, the elastomer is green and the aluminum yellow.

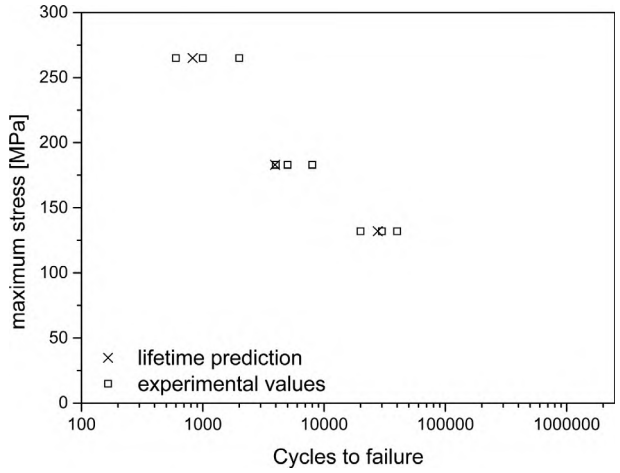

Fig. 12. Lifetime prediction and the experimental results for the aluminum layer in the laminate.

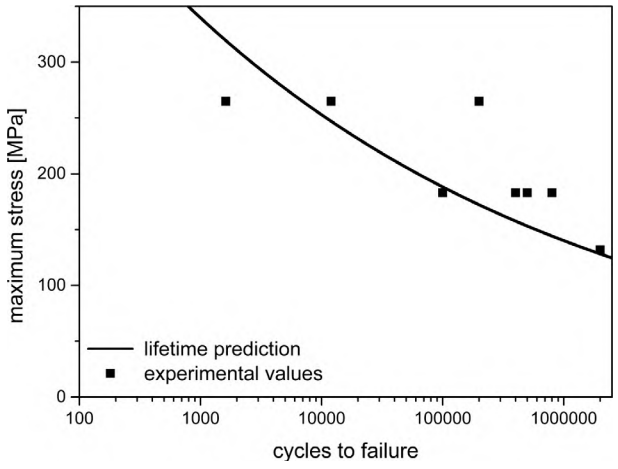

Fig. 13. S-N curve showing the lifetime prediction for the desired stiffness reduction and the obtained values in this research.

satisfactorily.

5.2. The influence of the elastomer interlayer

To describe the effect of the elastomer on the laminate, FML specimens were tested, which were identical to the FMEL specimens, except for the lack of elastomer interlayers. The FML failed at the lowest load level. This load level was omitted for the FMEL specimens due to a fatigue endurance limit higher than the 40% load level. The premature failure in the FML was caused by delamination in the metal-FRP interface.

Fig. 14. FML fatigue specimen loaded at 25% of UTS showing delamination and aluminum fractures.

Fig. 14 shows an FML specimen at the load level of 25% of UTS. The load was expected to be lower than the fatigue endurance limit, therefore no failure was estimated. However, the FML failed due to

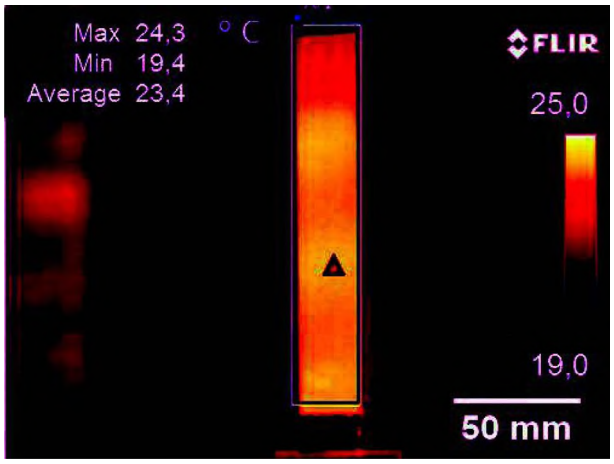

Fig. 15. Hot spots on the specimen highlighted through high contrast.

interfacial delamination in the first cycles. The interfacial shear stress, caused by a difference in stiffness of the constituents caused the delamination.

This delamination was inhibited by the elastomer layer in the FMEL through high ductility and improved adhesion. Although the elastomer interlayer did only carry minor loads, the integration of the layer was crucial for the laminate's fatigue properties.

5.3. Thermal imaging

Thermal imaging was used to monitor the temperature accumulation versus the given threshold of the specimen throughout the fatigue experiment. The accumulation was well below the threshold during the whole experiment.

The thermal imaging showed no breach of threshold, even though damage evolution caused friction. The temperature dependent mechanical properties of the polymers therefore were proven negligible when discussing the mechanical behavior of FMEL.

The thermal image at 100 000 cycles in Fig. 8(d) was taken after the failure criterion was met. Fig. 15 shows the same specimen with visible hot spots due to locally higher friction. This effect was anticipated to result from aluminum fracture and stress redistribution into the CFRP. The increase in stress therefore would result in higher friction and therefore temperature. The hot spots were examined post mortem using CT-scans. The scans proved the existence of aluminum cracks in the exact locations. Therefore the aluminum cracks could be linked to the locally higher temperature in the thermal imaging.

6. Conclusion

Fatigue testing was carried out on FMEL specimens according to ISO 13003, with a 20% stiffness degradation failure criterion. The experiments were accompanied with infrared thermal measurements and ex-situ CT-scans to assert the validity of the experiments and show the damage during testing.

A lifetime prediction for FMEL was not applicable and a combination of predictions for the constituents were used to formulate one prediction for the whole laminate. The prediction fit the experiment well for the failure criterion of 20% stiffness reduction.

The prominent stiffness drops in the fatigue experiments were correlated with cracks in the aluminum layer, which were detected and located by CT-scans. Additionally, areas of higher temperatures were measured via infrared thermal imaging and it was proven that locating cracks during the experiment was possible.

The FMEL exhibited high fatigue properties, because the fatigue endurance limit was above 40% of UTS. Also a high damage tolerance was observed, when a fracture in the aluminum did not cause a laminate failure or delamination, as it would be expected for FML.

Acknowledgements

The research of this paper is kindly financed by the Baden-Württemberg Stiftungs project "Faser-Metall-Gummi-Hybridlaminate (FMGL) ein neuartiges, nachhaltigesWerkstoffkonzept für den Fahrzeugleichtbau", support code MAT0012, which is part of the research program "Rohstoff- und Materialeffzienz in der Produktion". The authors kindly thank the Institute for Production Science (wbk) at the Karlsruhe Institute of Technology (KIT) for the production of the laminates. Also we would like to thank the Kraiburg Holding GmbH und Co. KG for the supply of the elastomer. The authors would like to thank Dr. Karl-Heinz Lang and Mr. Sebastian Höhne for their support and technical assistance.

References

[1] Vogelsang L, Vlot A. Development of fiber metal laminates for advanced aerospace structures. J Mater Process Technol 2000;2000(103):1–5.
[2] Vlot A, Gunnink J. Fibre metal laminates/an introdution. Netherlands: Springer Verlag; 2001.
[3] Sinmazcelik T, Avcu E, Bora M, Coban O. A review: fibre metal laminates, background, bonding types and applied test methods. Mater Des 2011(32):3671–85.
[4] Vermeeren C. An historic overview of the development of fibre metal laminates. Appl Compos Mater 2003;10(4–5):189–205.
[5] Laliberte JF, Poon C, Straznicky PV, Fahr A. Post-impact fatigue damage growth in fiber-metal laminates. Int J Fatigue 2002;24(2):249–56.
[6] Takamatsu T, Matsumura T, Ogura N, Shimokawa T, Kakuta Y. Fatigue crack growth properties of a glare3-5/4 fiber/metal laminate. Eng Fract Mech 1999;63(3):253–72.
[7] Homan J. Fatigue initiation in fibre metal laminates. Int J Fatigue 2006;28(4):366–74.
[8] Lin CT, Kao PW, Jen M-HR. Thermal residual strains in carbon fibre-reinforced aluminium laminates. Composites 1994(25):303–7.
[9] Müller B, Sinke J, Anisimov AG, Groves RM. Thermal strains in heated fiber metal laminates. In: Aggelis D, van Hemelrijck DG, editors. Emerging technologies in non-destructive testing VI. London: CRC Press; 2015. p. 205–11.
[10] Müller B, Teixeira De Freitas S, Sinke J. Thermal cycling fiber metal laminates: considerations, test setup and results. In: 20th International conference on composite materials.
[11] Stoll M, Weidenmann K. Characterization of interface properties of fiber-metal-laminates (fml) with optimized interfaces. In: Proceedings of 2nd international conference euroHybrid; 2016.
[12] Stoll M, Weidenmann K. The impact of environmental stress on the mechanical behavior of fiber-metal-laminates with elastomer interlayers (fmel). In: Proceedings of 17th European conference on composite materials; 2016.
[13] Sarlin E, Liu Y, Vippola M, Zogg M, Ermanni P, Vuorinen J, et al. Vibration damping properties of steel/rubber/composite hybrid structures. Compos Struct 2012;94(11):3327–35.
[14] Sarlin E, Apostol M, Lindroos M, Kuokkala V-T, Vuorinen J, Lepistö T, et al. Impact properties of novel corrosion resistant hybrid structures. Compos Struct 2014;108:886–93.
[15] Sarlin E, Hoikkanen M, Frisk L, Vuorinen J, Vippola M, Lepistö T. Ageing of corrosion resistant steel/rubber/composite hybrid structures. Int J Adhes Adhes 2014;49:26–32.
[16] Vermeeren CAJR. The application of carbon fibres in are all laminates. Tech rep, Delft University of Technology; 1991.
[17] Cortes P, Cantwell W. The tensile and fatigue properties of carbon fiber-reinforced peek-titanium fiber-metal laminates. J Reinf Plast Compos 2004;23(15):1615–23.
[18] Jen M, Tseng Y, Li P. Fatigue response of hybrid magnesium/carbon-fiber/peek nanocomposite laminates at elevated temperature (ii). In: Key engineering materials, vol. 334; 2007. p. 693–6.
[19] Jen M, Tseng Y, Li P. Fatigue response of hybrid magnesium/carbon-fiber/peek nanocomposite laminates at elevated temperature. 7 (Special_Issue); 2007. p. s56–s60.
[20] Austin T, Gregson P, Dakin J, Powell P, Singh M. Fatigue damage in carbon fiber reinforced aluminum alloy laminates. In: Proc of 5th int conf on deformation and fracture of composites; 1999. p. 191–200.
[21] Shim D, Alderliesten R, Spearing S, Burianek D. Fatigue crack growth prediction in glare hybrid laminates. Compos Sci Technol 2003;63(12):1759–67. http://dx.doi.org/10.1016/S0266-3538(03)00082-4.
[22] Nijssen R. Fatigue life prediction and strength degradation of wind turbine rotor blade composites. TU Delft, Delft University of Technology; 2006.
[23] Vassilopoulos A, Keller T. Fatigue of fiber-reinforced composites. Springer Science & Business Media; 2011.
[24] Luukkonen A, Sarlin E, Villman V, Hoikkanen M, Vippola M, Kallio M, et al. Heat generation in dynamic loading of hybrid rubber-steel composite structure. In: Proceedings of the 17th international conference on composite materials, Edinburgh, UK; 2009.

[25] Austin T, Singh M, Gregson M, Powell P. Characterization of fatigue crack growth and related damage mechanisms in frp - metal hybrid laminates. Compos Sci Technol 2008;2008(68):1399–412.
[26] Zangenberg J, Brøndsted P, Gillespie J. Fatigue damage propagation in unidirectional glass fibre reinforced composites made of a non-crimp fabric. J Compos Mater 2014;48(22):2711–27.
[27] Hwang W, Han K. Fatigue of composites—fatigue modulus concept and life prediction. J Compos Mater 1986;20(2):154–65.
[28] Baumert E, Johnson W, Cano R, Jensen B, Weiser E. Fatigue damage development in new fibre metal laminates made by the VARTM process. Fatigue Fract Eng Mater Struc 2011;34(4):240–9. http://dx.doi.org/10.1111/j.1460-2695.2010.01509.x.
[29] Alderliesten R, Rans C. The meaning of threshold fatigue in fibre metal laminates. Int J Fatigue 2009;31(2):213–22. http://dx.doi.org/10.1016/j.ijfatigue.2008.09.008.
[30] Alderliesten R, Schijve J, van der Zwaag S. Application of the energy release rate approach for delamination growth in glare. Eng Fract Mech 2006;73(6):697–709. http://dx.doi.org/10.1016/j.engfracmech.2005.10.006.
[31] Alderliesten R, Homan J. Fatigue and damage tolerance issues of glare in aircraft structures. Third Int Conf Fatigue Compos 2006;28(10):1116–23. http://dx.doi.org/10.1016/j.ijfatigue.2006.02.015.
[32] Alderliesten R. On the available relevant approaches for fatigue crack propagation prediction in glare. Int J Fatigue 2007;29(2):289–304. http://dx.doi.org/10.1016/j.ijfatigue.2006.03.003.
[33] Fibre-reinforced plastics – determination of fatigue properties under cyclic loading conditions. Standard, International Organization for Standardization, Geneva, CH; 2003.
[34] Radaj D, Vormwald M. Ermüdungsfestigkeit: Grundlagen für Ingenieure. Springer-Verlag; 2007.
[35] Basquin O. The exponential law of endurance tests, in: proc. ASTM, Vol. 10; 1910, p. 625.
[36] Suresh S. Fatigue of materials. Cambridge University Press; 1998.
[37] Hashin Z, Rotem A. A fatigue failure criterion for fiber reinforced materials. J Compos Mater 1973;7(4):448–64.
[38] Kawai M, Murata T. A three-segment anisomorphic constant life diagram for the fatigue of symmetric angle-ply carbon/epoxy laminates at room temperature. Compos Part A: Appl Sci Manuf 2010;41(10):1498–510.
[39] El Kadi H, Ellyin F. Effect of stress ratio on the fatigue of unidirectional glass fibre/epoxy composite laminae. Composites 1994;25(10):917–24.
[40] Adam T, Fernando G, Dickson R, Reiter H, Harris B. Fatigue life prediction for hybrid composites. Int J Fatigue 1989;11(4):233–7.
[41] Epaarachchi JA, Clausen PD. An empirical model for fatigue behavior prediction of glass fibre-reinforced plastic composites for various stress ratios and test frequencies. Compos Part A: Appl Sci Manuf 2003;34(4):313–26.
[42] Ogin S, Smith P, Beaumont P. Matrix cracking and stiffness reduction during the fatigue of a (0/90) s gfrp laminate. Compos Sci Technol 1985;22(1):23–31.
[43] Whitworth H. A stiffness degradation model for composite laminates under fatigue loading. Compos Struct 1997;40(2):95–101.
[44] Garcea S, Mavrogordato M, Scott A, Sinclair I, Spearing S. Fatigue micromechanism characterisation in carbon fibre reinforced polymers using synchrotron radiation computed tomography. Compos Sci Technol 2014;99:23–30.
[45] Garcea S, Sinclair I, Spearing S. In situ synchrotron tomographic evaluation of the effect of toughening strategies on fatigue micromechanisms in carbon fibre reinforced polymers. Compos Sci Technol 2015;109:32–9.
[46] Jespersen K, Wang Y, Zangenberg J, Lowe T, Withers P, Mikkelsen L. Ex-situ time-lapse X-ray ct study of 3d micro-structural fatigue damage evolution in uni-directional composites.
[47] Sarlin E. Characterisation of novel corrosion resistant stainless steel/rubber/composite hybrid structures. Tampere University of Technology; 2014.
[48] Fleischer J, Roth S, Sommer C. Faser-metall-gummi-hybridlaminate. ZWF Zeitschrift für wirtschaftlichen Fabrikbetrieb 2016;9:483–6.
[49] Stoll M, Weidenmann K. Materials selection for a fiber-metal-laminate with elastomer interlayers. In: Proceedings of 21st international conference on composite materials, Xi'an, China; 2017.
[50] Ashby MF. Materials selection in mechanical design. Metall Ital 1994;86:475.
[51] Bestimmung der Zugeigenschaften – Teil 5: Pruefbedingungen fuer unidirektional faserverstaerkte Kunststoffverbundwerkstoffe. Standard, European Committee for Standardization, Brussels, BE; 1997.